The Effect of Cohesive Forces on the Fluidization of Aeratable Powders

Janine E. Galvin
National Energy Technology Laboratory, Albany, OR 97321

Sofiane Benyahia
National Energy Technology Laboratory, Morgantown, WV 26507

DOI 10.1002/aic.14307
Published online December 12, 2013 in Wiley Online Library (wileyonlinelibrary.com)

The effects of cohesive forces of van der Waals type in the fluidization/defluidization of aeratable type A powders in the Geldart classification are numerically investigated. The effects of friction and particle-size distribution (PSD) on some design-significant parameters, such as minimum fluidization and bubbling velocities, are also investigated. For these types of particles, cohesive forces are observed as necessary to fully exhibit the role friction plays in commonly observed phenomena, such as pressure overshoot and hysteresis around minimum fluidization. This study also shows that a full-experimental PSD consisting of a dozen particle sizes may be sufficiently represented by a few particle diameters. Reducing the number of particle types may benefit the continuum approach, which is based on the kinetic theory of granular flow, by reducing computational expense, while still maintaining the accuracy of the predictions. Published 2013 American Institute of Chemical Engineers *AIChE J*, 60: 473–484, 2014
Keywords: cohesive forces, Geldart A powder, fluidization cycle, polydispersity, friction forces, discrete particle method

Introduction

Small type A powders, as classified by Geldart,[1] are of great importance in industry. These powders offer many advantages over other powder types due to the ease of fluidization and the large surface area of the particles. Such features often make these powders the ideal choice for reacting particles (e.g., pulverized coal combustion and gasification) or as solid catalysts for chemical reactions (e.g., fluid catalytic cracking or FCC). Experimentally, the cohesiveness of a powder and its fines content are known to play an important role in the rheological and fluidization behavior of type A powders.[2] In fact, Molerus[3] attributed the transition from group C to A and A to B in the Geldart classification of powders to the diminishing strength of cohesive van der Waals forces. Furthermore, simple experiments of free-falling type A powders clearly showed the effects of van der Waals cohesive forces in creating agglomerates of small particles.[4]

The importance of cohesive forces on homogenous (i.e., nonbubbling) bed expansion during fluidization of type A particles has been the subject of debate as Girimonte and Formisani[5] summarized. In particular, Jackson[6] concluded that the stable expansion of such beds cannot be based on hydrodynamics alone as the solid-like behavior of the bed during this transition period indicates sustained particle–particle contacts must exist. Therefore, cohesive forces have been reported to play some role in maintaining a stable regime between minimum and bubbling fluidization.[5] Another experimentally observed effect at minimum fluidization is a spike in pressure drop that extends beyond the static pressure of the bed. For type B particles, this behavior has been explained by the interlocking of these coarser particles (such as uniformly sized sharp sand) that requires an extra force to unlock them.[7] For type A particles, Jackson[6] cited friction as the main cause of the spike because increasing the bed diameter decreases the amplitude of the pressure spike. Jackson[6] indicated that further measurements are needed to distinguish between the effects of wall friction and cohesion. Isolating the effects of cohesive van der Waals forces from other effects, such as electrostatics and humidity, however, is very difficult to do experimentally. Accordingly, computations offer a useful alternative for isolating and consequently understanding the effects of cohesion; one can simply neglect specific forces by not including them in the model. The major objective of this work is to investigate the effect of cohesion on the fluidization and defluidization of small particles using a computational fluid dynamic (CFD) approach.

The majority of researchers using a continuum two-fluid model (TFM), based on kinetic theory for granular flows (KTGF), have ignored cohesion. However, a few exceptions exist.[8–10] For example, van Wachem and Sasic included cohesive force calculations in a simple force balance, with assumptions, to determine the size of cohesive agglomerates.[9] This information was then used to feed into their TFM simulation. In a different approach, Gidaspow and Huilin included the effects of cohesive forces for a FCC catalyst, a

Correspondence concerning this article should be addressed to S. Benyahia at Sofiane.Benyahia@netl.doe.gov.

typical group A powder, via the radial distribution function at contact.[8] Ye et al. later investigated possible modifications to KTGF based on discrete particle simulations of the same type of particles in a fully periodic system in a vacuum. Similar to the work of Gidaspow and Huilin,[8] they independently found that the effects of cohesion could be included in the radial distribution function.[10] A discrete particle approach, wherein the trajectory and collision of every particle in the computational domain is resolved, circumvents the difficulties encountered in continuum models when it comes to incorporating cohesive forces. Conversely, the ease of including forces in discrete methods is largely offset by the greater computational demands involved in the calculations of tracking each particle and its neighbors and resolving their collisions. The large number of particles is a major constraint in conducting DPM simulations especially when dealing with small type A particles. As a result, different strategies have been adopted to reduce the computational requirements. For example, studies have used larger particles with low density[11] or used artificially high cohesive force on larger particles.[12,13] Regardless, small system geometries are typically still used to obtain numerical results in a reasonable time (e.g., Wang et al.[14]). The current study is similarly restricted.

Recent numerical studies from Kuipers' research group[14] concluded that the effects of cohesive van der Waals forces were not significant in a small pseudo three-dimensional (3-D) fluidized bed with FCC particles of 75-μm diameter. In one study,[15] the gas inlet velocity was about 10 times the minimum fluidization velocity (U_{mf}), and the values for material property of cohesion (Hamaker constant) were relatively low compared to those reported in the literature.[16–18] In this study, full 3-D simulations of a fluidized bed are conducted along the complete fluidization/defluidization cycle using reasonable material cohesion properties and realistic particles with asperities on their surface. The effects of friction and particle-size distribution (PSD) on key design parameters, such as minimum fluidization and bubbling velocities, are examined. The results of these studies are used to assess the overall effects of cohesive forces in the fluidization of small type A powders.

Model Description

The effect of cohesion on the flow behavior of small Geldart type A powders is explored using DPM-CFD simulations. In this approach, the fluid phase is described by the standard volume-averaged Navier–Stokes equations for a single phase modified to include the presence of the particulate phase, which is modeled using discrete particles. Accordingly, the continuum gas-phase governing equations for mass and momentum conservation in a nonreacting isothermal system are as follows

$$\frac{\partial\left(\rho_g\varepsilon_g\right)}{\partial t}+\nabla\cdot\left(\rho_g\varepsilon_g\mathbf{V}_g\right)=0 \tag{1}$$

and

$$\left[\frac{\partial\left(\rho_g\varepsilon_g\mathbf{V}_g\right)}{\partial t}+\nabla\cdot\left(\rho_g\varepsilon_g\mathbf{V}_g\mathbf{V}_g\right)\right]=-\varepsilon_g\nabla P_g+\nabla\cdot\boldsymbol{\tau}_g -\sum_{p=1}^{N_T}\beta_p\frac{\varphi_p}{\varphi_c}\left(\mathbf{V}_g-\mathbf{V}_p\right)+\varepsilon_g\rho_g\mathbf{g} \tag{2}$$

where ε_g is the fluid void fraction, ρ_g is the fluid-phase density, P_g is the fluid-phase pressure, $\boldsymbol{\tau}_g$ is the fluid viscous stress tensor, $\mathbf{g}$ is the specific gravity force, $\mathbf{V}_g$ is the local average velocity of the fluid phase, $\mathbf{V}_p$ is the particle velocity, β_p is the interphase momentum exchange coefficient, N_T represents the total number of particles in the system, and ϕ_p and ϕ_c are volume of the particle and fluid cell, respectively.

The averaging process yields unknown terms, which require constitutive relations in terms of the flow field variables to establish a fully specified set of equations. Those terms include the fluid viscous stress tensor and the interphase momentum exchange term (or drag force). Closure for the fluid-phase viscous stress tensor is achieved by assuming a Newtonian fluid, in which case, the viscous stresses are proportional to the rate-of-strain

$$\boldsymbol{\tau}_g=2\mu_g\mathbf{D}_g-\frac{2}{3}\mu_g\left(\nabla\cdot\mathbf{V}_g\right)\mathbf{I}\ \text{and}\ \mathbf{D}_g=\frac{1}{2}\left(\nabla\mathbf{V}_g+\left(\nabla\mathbf{V}_g\right)^t\right) \tag{3}$$

where μ_g is the fluid viscosity, $\mathbf{D}_g$ is the rate-of-strain tensor, and $\mathbf{I}$ is the identity tensor. Coupling with the particulate phase is achieved primarily through the drag force, which is closed using the standard model by Wen–Yu[19] for the interphase momentum exchange coefficient

$$\beta_p=\frac{3}{4}C_D\frac{\rho_g\varepsilon_g|\mathbf{V}_g-\mathbf{V}_p|}{d_p}\varepsilon_g^{-2.65} \tag{4}$$

where d_p is the particle diameter, and C_D is the drag coefficient expressed as

$$C_D=\begin{cases}24/\mathrm{Re}\left(1+0.15\mathrm{Re}^{0.687}\right) & \mathrm{Re}<1000\\ 0.44 & \mathrm{Re}\geq 1000\end{cases}\qquad \text{and}\ \mathrm{Re}=\frac{\rho_g\varepsilon_g|\mathbf{V}_g-\mathbf{V}_p|d_p}{\mu_g} \tag{5}$$

In the DPM-CFD approach, the particulate phase is represented by N_T spherical particles with diameter d_p and density ρ_p. The motion of each individual particle is described using Newton's laws of motion

$$\frac{d\mathbf{x}_p}{dt}=\mathbf{V}_p \tag{6}$$

$$\frac{d\mathbf{V}_p}{dt}=\mathbf{g}-\frac{\nabla P_g}{\rho_p}+\frac{\beta_p}{\rho_p}\left(\mathbf{V}_g-\mathbf{V}_p\right)+\frac{\mathbf{F}_{c,p}}{m_p}+\frac{\mathbf{F}_{vw,p}}{m_p} \tag{7}$$

$$I_p\frac{d\boldsymbol{\omega}_p}{dt}=\mathbf{T}_p \tag{8}$$

where $\mathbf{x}_p$ is the particle position, $\mathbf{F}_{c,p}$ is the net contact force due to particle contact with walls and other particles, $\mathbf{F}_{vw,p}$ is the net van der Waals force arising from particle–particle and particle–wall interactions, I_p is the moment of inertia, $\boldsymbol{\omega}_p$ is the particle angular velocity, and $\mathbf{T}_p$ is the sum of all torques acting on the particle. The other terms are as defined earlier.

The contact force from particle–particle or particle–wall collisions is described using a soft-sphere model based on the spring-dashpot model by Cundall and Strack.[20] In this approach, a linear spring and a dashpot are used to formulate the normal contact force, whereas a linear spring, a dashpot, and a slider are used to compute the tangential contact force. The spring accounts for repulsion between colliding particles, and the dashpot dissipates kinetic energy due to inelastic

collisions. The slider accounts for finite Coulomb friction between particles and serves to limit the tangential contact force when sliding occurs. (For more specific details on the model and its implementation, see Garg et al.[21])

Interparticle forces can result from a variety of causes (e.g., capillary forces and electrostatic forces).[22] Of interest in this article are those forces arising from van der Waals interactions. The van der Waals forces between particles have their origin in the forces between constituent molecules (e.g., dipole–dipole, dipole-induced-dipole, etc.), and a rigorous treatment requires a quantum mechanics description. These molecular interactions are generally quantified via interaction potentials that show an inverse power dependence on the separation distance. The interaction potentials are then used, with simplified treatments, to obtain an expression for the macroscopic interparticle attractive force. For example, Hamaker[16] approximated the macroscopic van der Waals interparticle attractive force between various geometric shapes by summing all pairwise combinations of corresponding intermolecular attraction forces between the two bodies in a vacuum. Using this analysis, the magnitude of the van der Waals force between two spheres of different radii (r_p and r_l) with smooth surfaces is as follows

$$F_{\mathrm{vdw,lp}} = \frac{A}{3}\frac{2r_p r_l\left(r_p+r_l+s\right)}{s^2\left(2r_p+2r_l+s\right)^2}\left[\frac{s\left(2r_p+2r_l+s\right)}{\left(r_p+r_l+s\right)^2-\left(r_p-r_l\right)^2}-1\right]^2 \tag{9}$$

where A is the Hamaker coefficient, which is a constant that depends on the material properties with typical values ranging from $10^{-20}-10^{-19}$ J.[16–18] The quantity s is the distance between their surfaces

$$s=\left(r_p+r_l\right)-\left|\mathbf{x}_p-\mathbf{x}_l\right| \tag{10}$$

where $\mathbf{x}_p$ and $\mathbf{x}_l$ denote the position of particle p and l, respectively. In the limit that s is much less than either particle radii ($s \ll r_p, r_l$), this expression reduces to the more familiar expression[18]

$$F_{\mathrm{vdw,pl}} = \frac{Ar_{pl}}{12s^2} \tag{11}$$

where $r_{pl}=\frac{2r_p r_l}{r_p+r_l}$ is the average particle radius.

As evident, the van der Waals force decreases with decreasing particle size. However, the magnitude of other forces in the system, such as gravity and drag, decrease to a greater extent.[23] Consequently, the van der Waals force can be dominant for very small particles even though the force is smaller in magnitude than for larger particles of the same material. Moreover, the van der Waals forces are only noticeable when the particles are sufficiently close together, that is, when the separation distances are small, as the van der Waals force drops rapidly with increasing distance. The analogous attractive force for a system consisting of a sphere and a flat surface (i.e., wall) is effectively twice that[16,18]

$$F_{\mathrm{vdw,pw}} = \frac{Ar_p}{6s^2} \tag{12}$$

Strictly speaking, neither the molecular forces are pairwise additive nor can the additive approach be readily extended to bodies interacting in a medium. Nonetheless, the Hamaker model is commonly invoked for investigating the effects of interparticle cohesion and enables us to gain a better understanding of the importance of such forces.

If surface asperities or protuberances exist, they will impact the real area of contact and distance between the bulk surfaces.[24] Real particles will be characterized by some finite surface roughness. In idealized geometries, such as spheres, surface roughness may limit the approach of the two particles so that the effective separation distance is larger, and as a result, the van der Waals attraction is reduced.[23] Surface structures may also give rise to mechanical interlocking of the surfaces. A rigorous study of the contact problem for real particles with rough surfaces is a challenging issue not addressed here (see Adams and Nosonovsky[25] for more details). In addition, mathematical representations of varying complexity have been proposed to describe particle surface topography, from invoking a statistical distribution of asperity heights to models based on fractal surface geometries.[22] The application of such models to interparticle forces is another difficult problem. As a result, simpler asperity contact models have been developed.

A model commonly used to describe the van der Waals force, while accounting for the effect of surface roughness was developed by Rumpf.[26] This model is based on contact of a single hemispherical asperity centered at a flat surface and interacting with a much larger spherical particle. The model consists of two terms. The first represents the interaction of the spherical particle with the asperity, whereas the second describes the interaction between the spherical particle and the flat surface, which is separated by the height (radius) of the asperity. Rumpf[26] obtained his modified Hamaker model based on Lifshitz's macroscopic approach[27,28] and applying Derjaguin's approximation for both interactions.[24] Note that, the Derjaguin's approximation is only valid when $s \ll r_p, r_l$ (i.e., the surface-to-surface separation is much smaller than either particle radii).[18] Rumpf's original expression[26] for the attractive force was extended for a system consisting of an asperity centered on the surface of the spherical particle interacting with another spherical particle of different radii, and when the asperity height is not too far from the average sphere radius[29]

$$F_{\mathrm{vdw,pl}} = \frac{Ar_{\mathrm{pl}}}{12s^2}\left(\frac{1}{1+r_{\mathrm{pl}}/r_{\mathrm{asp}}}+\frac{1}{\left(1+r_{\mathrm{asp}}/s\right)^2}\right) \tag{13}$$

where r_{asp} is the radius of the asperity. Asperities of radii ranging from 0.1–0.5 μ for particle diameters ranging from the order of 1 μ to 10's of microns have been reported in the literature. Also, the radius of an asperity is usually lower for used particles than for fresh particles due to abrasion.[30] Rabinovich et al.[24] further modified this model to include a more realistic quantification of surface topography through the root-mean square of the surface roughness.

Similar to Rumpf,[29] Forsyth and Rhodes[31] also developed a model for a single hemispherical asperity centered on the surface a larger spherical particle interacting with a flat surface. This expression is shown here, modified for a system of interacting spherical particles

$$F_{\mathrm{vdw,pl}} = \frac{Ar_{\mathrm{pl}}}{12s^2}\left(\frac{r_{\mathrm{asp}}/r_{\mathrm{pl}}}{\left(1+s/2r_{\mathrm{asp}}\right)^2}+\frac{1}{\left(1+r_{\mathrm{asp}}/s\right)^2\left(1+s/2r_{\mathrm{pl}}+r_{\mathrm{asp}}/2r_{\mathrm{pl}}\right)^2}\right) \tag{14}$$

A comparison of these different models, namely, the complete Hamaker and reduced Hamaker expressions (Eqs. 9

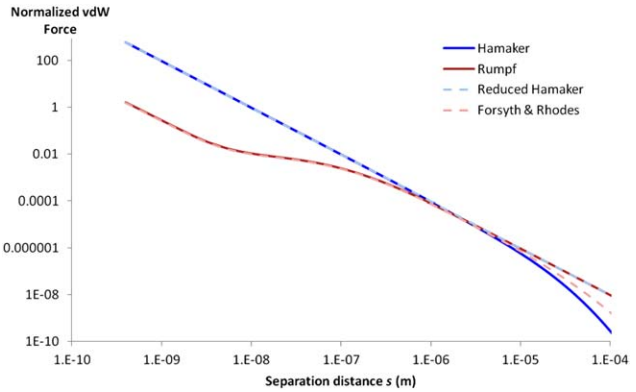

Figure 1. Normalized van der Waals (vdW) force with the weight of a particle (75-μm diameter and 0.1-μm asperities) as a function of interparticle distance for different cohesion models.

[Color figure can be viewed in the online issue, which is available at wileyonlinelibrary.com.]

and 11, respectively), the Rumpf expression[29] (Eq. 13), and the Forsyth and Rhodes expression[31] (Eq. 14), is given in Figure 1. This figure shows the normalized van der Waals force, defined as the ratio of interparticle attractive force ($F_{\mathrm{vdw,lp}}$) to particle weight (mg), as a function of separation distance (s) for the case of equal-sized spherical particles with typical values for parameters: $A = 10^{-19}$ J, $r_p = 35$ μm, $\rho = 1.5$ g/cm^3, and $r_{\mathrm{asp}} = 0.1$ μm. It is worth noting that the dimensionless van der Waals force is commonly used to quantify cohesiveness and is also referred to as the cohesive granular bond number.[22]

The main difference between the two Hamaker expressions for the interparticle force and those of Rumpf,[29] and Forsyth and Rhodes[31] is in the effects of asperities. As is evident in Figure 1, surface irregularities may reduce the evaluated cohesive forces by about two orders of magnitude near contact. In contrast, the differences between these models observed at large distances, although still large, are irrelevant due to the very weak nature of these forces (less than 10^{-6} the weight of a particle). Also worth noting is that evaluation of the interparticle attractive force is very sensitive to the surface asperities, the effect of which is only crudely estimated in the selected models through interaction of a single spherical cap. Recall, for example, that in real surfaces the asperities are likely the sites where contact occurs. As the interparticle attractive force will vary depending on the size of the asperity, a range of forces are possible for a given particle with realistic surface roughness. For very small asperities, 0.01 μm for 10–100 μm particles, the contribution of the asperity to the total attractive force becomes insignificant.[32] Moreover, for realistic surface topographies, very small asperities will likely be overshadowed by larger asperities, that is, they are unlikely to participate in contact anyway.[33]

As discussed above, different approaches are available to quantify the van der Waals force. In this effort, the extended expression of Rumpf[29] (Eq. 13) is used to evaluate all particle–particle and particle–wall cohesive interactions. The force of interaction between a particle and a wall is calculated from the same expression (Eq. 13) but taking $r_p = r_l$ in the definition of r_{pl} and multiplying the equation by a factor of 2. The net van der Waals force on the particle is then given by the sum of all particle–particle and particle–wall cohesive interactions

$$\mathbf{F}_{\mathrm{vw,p}} = \sum_{p=1}^{N_c} -\mathbf{F}_{\mathrm{vdw,pl}}\,\mathbf{n}_{\mathrm{pl}} \tag{15}$$

where $\mathbf{n}_{\mathrm{pl}}$ is the unit vector along the line of contact pointing from particle p to particle l, and N_c represents the number of cohesive particle–particle and particle–wall interactions. As discussed above, the model chosen here to represent surface roughness can only be considered an approximation. A more accurate model would need to include not only a rigorous description of surface roughness but also the effects of particle hardness (deformation), which is beyond the scope of the current work.

The Multiphase Flow with Interphase eXchange (MFIX) code (https://mfix.netl.doe.gov) is used for all simulations in this effort. The gas-phase flow field is solved numerically on a staggered Cartesian computational grid using a semi-implicit scheme based on the well-known SIMPLE algorithm[34] with a variable time step. The convection terms are evaluated using Superbee, a second-order discretization scheme, along with deferred correction.[35] In contrast, the particle equations of motion do not require a computational grid, and a constant time step is used. As has been used for similar systems, the DPM time step is equal to 1×10^{-6} s.[11,15,36] The particle velocity is updated through a first-order integration scheme, which is in turn used to update the particle's position. In this DPM-CFD coupled approach, the simulation effectively advances in two steps. First, the continuum fluid equations are solved for a fluid time step, wherein the particles are stationary. Once the fluid variables converge, the discrete particle simulation begins, wherein the particles are advanced through several smaller time steps until the time elapsed equals a fluid time step. At this point, the fluid and particles are at the same physical time and the process repeats.

Note that, in the drag force relation (Eqs. 4 and 5) used to calculate the drag force on the particle, the mean gas-phase velocity is interpolated to the particle location. The drag force on the fluid is then calculated by projecting the drag force on each particle back onto to the gas-phase Cartesian grid.

Simulation Conditions

The DPM-CFD model described above is used to simulate the fluidization and defluidization process of a small 3-D bed of Geldart group A particles. Unless otherwise noted, the input parameters for these simulations, including gas and particle properties, system geometry, and numerical parameters are summarized in Table 1 and discussed briefly below. Note that, the gas (air) flow is treated as slightly compressible so the gas-phase density is described using the ideal gas law as the equation of state. A monodisperse system composed of spheres that are 75 μm in diameter and 1500 kg/m^3 in density is considered first. The effects of PSD are also investigated with two polydisperse systems having the same overall mean particle size as the monodisperse system (75 μm) but composed of either three or 12 particle types of different diameter and identical density. The simulated PSD by mass for the two polydisperse systems is presented in Table 2. The size distribution consisting of 12 particle types was taken from experimental data for an FCC powder given by the first PSRI (Particulate Solids Research Inc.) challenge problem.[37] The size distributions consisting of one and three

Table 1. Simulation Conditions Including Gas and Solids Physical Parameters

Quantity	Symbol	Units	Value
Gravitational acceleration	g	m/s^2	9.81
Gas viscosity	μ_g	Pa s	1.8×10^{-5}
Gas temperature and pressure	T_g, P_G	K, Pa	300, 101,300
Particle density	ρ_p	kg/m^3	1500
Particle (mean) diameter	d_p	μm	75
Total number of particles	N_t	–	90,000, 119,726, 128,550
Normal spring constant	k_n	kg/s^2	7
Normal restitution coefficient	e_n	–	0.95
Friction coefficient	μ	–	0.3
Hamakar constant	A	J	10^{-19}
Radius of asperity	r_{asp}	μm	0.1
Minimum cutoff distance	s_{min}	nm	0.4
Maximum cutoff distance	s_{max}	μm	20
System geometry	$L_x \times L_y \times L_z$	cm × cm × cm	0.3 × 1.0 × 0.3
Cartesian grid	$i \times j \times k$	–	12 × 40 × 12

The particle diameter represents the mean particle diameter in the polydisperse case. The total number of particles varies depending on the size distribution, with the total number of particles increasing with the width of the size distribution.

particle types are an approximation of the real PSD having the same mean particle size. Accordingly, whether a simulation with fewer particle types may be used and still accurately reproduce the results from a simulation using a more complete experimental PSD is also investigated.

Five parameters are required to describe the contact force in this soft-sphere model: the normal and the tangential spring stiffness (k_n and k_t), the normal and the tangential damping coefficient (η_n and η_t), and the friction coefficient (μ). Note that the normal dashpot damping coefficient can be related to the normal restitution coefficient (e_n) using the differential equations for a damped harmonic oscillator.[38,39] In addition, the tangential collisional parameters are related to the normal collisional parameters, wherein the ratio of normal to tangential spring constant (k_n/k_t) is taken as 2/7.[38,40] Similar to the work by Silbert et al.,[40] the ratio of normal to tangential dampening coefficient (η_n/η_t) is taken as 1/2. The values for normal and tangential particle–particle collisional parameters are the same as those for particle–wall interactions.

Note that, the interparticle attractive force (Eq. 13) approaches infinity as separation distance approaches zero (i.e., particle contact). To avoid this issue, a minimum cutoff separation (s_{min}) is used. For anything below this distance ($s \leq s_{min}$), the van der Waals force remains constant and is assumed to equal to the force experienced at s_{min}. As evident from Figure 1, the van der Waals force drops rapidly with increasing separation. Therefore, to save computational time, a maximum cutoff separation is also used (s_{max}), beyond which the cohesive force is ignored. In this case, s_{max} is approximately equal to the particle diameter divided by four. In this effort, the particle roughness is assumed to be characterized by an asperity of radius 0.1 μm, which is slightly less than the reported 0.15-μm asperity radii for small FCC particles.[32,41]

Table 2. Particle-Size Distribution for Polydisperse Cases Containing 12 and Three Particle Types

Bin Number	Particle Diameter (μm)	Weight (%)	Number of Particles
1	*44/54*	*5/30*	*22286/72337*
2	*49/75*	*5/40*	*16136/35999*
3	*54/100*	*5/30*	*12056/11390*
4	58	10	19460
5	61	5	8364
6	65	10	13826
7	72	10	10173
8	77	10	8317
9	84	10	6406
10	92	10	4876
11	100	10	3797
12	110	10	2853

The first three rows contain information about the powder with ternary PSD (indicated by numbers in italic).

The simulations are run using a 3-D domain in Cartesian coordinates. In regard to gas-phase continuum equations, the four sidewalls (east, west, front, and back) are treated as impenetrable noslip boundaries (the normal and tangential components of gas velocity are zero). At the outlet, the pressure is specified atmospheric (1.013×10^6 Pa). A uniform superficial gas velocity is specified at the inlet, which is set to change with time to examine the fluidization/defluidization process. Following Ye et al.,[36] the superficial gas velocity is changed linearly in time rather than using a stepwise increment method

$$U_{sf} = Kt \tag{16}$$

where K is a constant value for acceleration/deceleration, and t is the simulation time. In this effort, a value of K equal ± 1 cm/s^2 is used for fluidization/defluidization, which is slightly smaller than the value used in a similar setup.[36] These authors selected a value of 3 cm/s^2 to achieve reasonable speed-up compared to the stepwise method, while minimizing differences in the predicted results (pressure drop and bed height). Ye et al.[36] discuss this matter in greater detail. Based on a brief investigation, the current results were also found to be insensitive to the particular technique for the value of K selected (figure not shown).

The initial state of a simulation is obtained by orderly placing particles at the bottom of the bed. The bed is then uniformly fluidized with air at a superficial gas velocity set at 1.2 cm/s ($\sim 2.4 U_{mf}$ for the monodisperse case) allowing it to bubble/fluidize. After 0.2 s for the monodisperse case or 1 s for the polydisperse case, the superficial gas velocity is quickly decreased to zero over a span of 0.1 s causing the particles to drop and the bed to reach a packed state. This procedure allows for an initial random packing of particles and is referred to as the prefluidization stage. The prefluidization stage for the polydisperse case is longer to allow for particles with different sizes to naturally segregate (as shown later). The superficial gas velocity is then slowly increased ($K = 1$ cm/s^2) to about 2.5−3 U_{mf} during the fluidization stage and then decreased back to zero in the same manner

($K = -1$ cm/s^2) during the defluidization stage. This process, fluidization and defluidization, generally takes about 3 s.

During the fluidization and defluidization cycle, the pressure drop and bed height are measured to observe the impact of van der Waals-type cohesive forces on the fluidization behavior. The pressure drop across the bed (ΔP) is estimated by the pressure at the lowest computational node minus the pressure at the outlet, which is simply the atmospheric pressure. The pressure drop is then normalized (ΔP^*) by the weight of the particles per unit cross-sectional area of the bed ($\frac{m_{\text{tot}}\, g}{Area}$ where $m_{\text{tot}} = \sum_{p=1}^{Nt} \rho_p v_p$ and v_p is the particle volume). The bed height (H) is defined as the y-position (height) of the particle, below which 99% of the total mass is located. This method is very accurate and provides a smooth profile in bed height vs. superficial gas velocity and relies on the inherent nature of the discrete simulation data. Alternatively, the bed height may be defined as the grid height, below which contains a given percentage (e.g., 95 or 99%) of the bed weight (e.g., Syamlal and O'Brien[42]). This technique has been used in processing two-fluid simulations but in the DPM-CFD approach results in a staircase-type profile due to the discrete nature of the computational grid. A third approach uses the solids volume fraction in each cell and corresponding cell height to estimate an average bed height (e.g., Goldschmidt et al.[43]). This method yields a relatively smooth profile in comparison but still reflects a TFM approach in using grid based data. For all cases, the bed height is normalized (H^*) by the height of the bed measured at the start of the fluidization cycle corresponding to the monodisperse case with $d_p = 75$ μm, $A = 10^{-19}$J, $r_{\text{asp}} = 0.1$ μm, and $\mu = 0.3$, in which $H/\ d_p = 50.4$.

Fluidization of Cohesive Particles

The primary focus of this effort is how van der Waals-type cohesive forces affect the fluidization behavior of Geldart group A powders. Geldart[1] divided the fluidization behavior at ambient conditions according to particle size and density differences. Four behavior groups were recognized. Designated as group A are powders that give a region of homogenous nonbubbling fluidization beginning at the minimum fluidization velocity followed by bubbling fluidization as fluidization velocity increases. The minimum fluidization velocity (U_{mf}) is generally defined as the superficial fluid velocity, at which the drag force on the bed with $\varepsilon = \varepsilon_{\text{mf}}$ matches the buoyant weight of the bed. Geldart[1] also defined the minimum bubbling velocity (U_{mb}) as the superficial gas velocity, at which the first clearly recognizable bubble appears. Accordingly, group A particles are those for which $U_{\text{mb}}/U_{\text{mf}} > 1$. This behavior can be observed in Figure 2, which shows predicted fluidization behavior, namely, the nondimensional pressure drop and bed height during the process of fluidization and defluidization, for a system of noncohesive monodisperse particles.

Graphical determination of the minimum fluidization and minimum bubbling velocity from the fluidization/defluidization curves may vary. For example, some efforts identify the minimum fluidization velocity as the point, at which the pressure drop first equals the weight of the particles.[36,44] The minimum fluidization condition can also be marked by a discontinuous change in slope of both pressure drop and bed height curve.[6] A similar approach is used here, specifically, by marking the minimum fluidization condition as a sudden

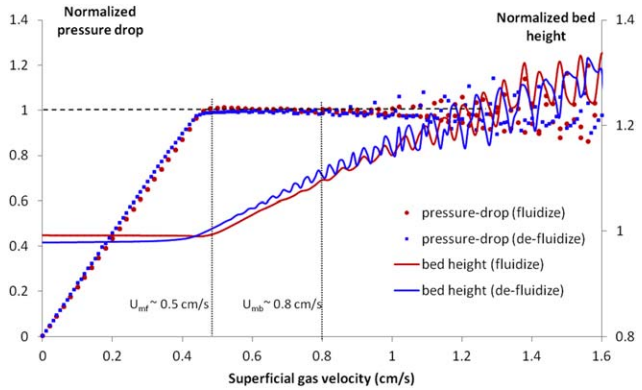

Figure 2. Fluidization/defluidization curves for a noncohesive ($A = 0$) monodisperse powder.

Characteristic parameters are: $d_p = 75$ μm and $\mu = 0.3$. The normalized pressure drop and bed height are represented by symbols and continuous lines, respectively. [Color figure can be viewed in the online issue, which is available at wileyonlinelibrary.com.]

change in the slope of bed height during fluidization, which gives a minimum fluidization velocity of 0.5 cm/s. The minimum bubbling velocity may be identified by the point, at which bubbling first begins through a visual inspection of the bed (or in snapshots).[11,45] It has also been identified by noting a change in the spatial fluctuation of local porosities,[36] or by the point where the hysteresis loop closes.[6] In this effort, the minimum bubbling velocity is defined as the point during fluidization when fluctuations in bed height begin to occur, which coincides with the appearance of bubbles in the bed. Using this approach, a minimum bubbling point may be identified at a superficial velocity of 0.8 cm/s. In agreement with earlier reports,[11,46] the results show that group A behavior may be predicted ($U_{\text{mb}}/U_{\text{mf}} > 1$) in the absence of interparticle forces. However, the precise behavior may still differ from that of real powders because the interparticle forces were explicitly set to zero in this case.

Figure 2 shows that the fluidization and defluidization curves track one another closely and only a slight hysteresis is evident, with the differences more prominent in the bed height curves than the pressure drop curves. Also worth noting are the large fluctuations in the curves of pressure drop and bed expansion height that occur when the superficial gas velocity is increased beyond the minimum bubbling velocity. This behavior is in contrast to what was observed experimentally,[47] which showed little fluctuation attributable to the relatively large bed used for the experiment. Recall that this and other simulation studies[36,48] use relatively small beds due to computational limitations on the number of simulated particles. These simulation studies also show large fluctuations resulting from the formation of large bubbles (relative to the bed diameter).

Figure 3 illustrates the effect of cohesion for the same system as Figure 2. Most notably, simulations without cohesion show a very small pressure overshoot, whereas simulations with cohesion show a clear pressure overshoot. This suggests that cohesion is a factor leading to the overshoot. In contrast, Ye et al.[36] observed a clear spike in pressure drop near U_{mf} without cohesion. Another simulation study,[48] however, detected only a small spike in pressure drop without cohesion and a much larger spike with cohesion, which is similar to present findings. This behavior was also confirmed in another

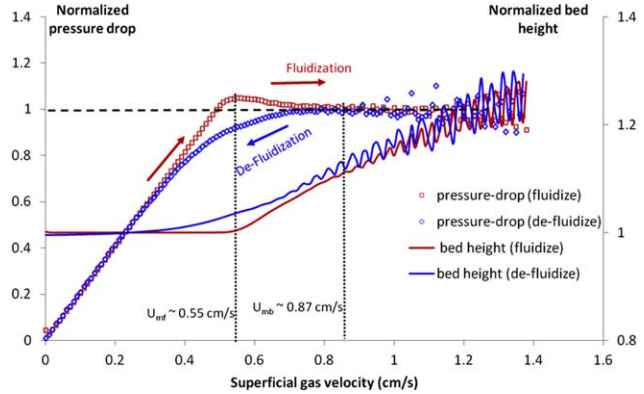

Figure 3. Fluidization/defluidization curves for a cohesive ($A = 10^{-19}$ J and $r_{asp} = 0.1$ μm) monodisperse powder.

Other properties as in Figure 2. [Color figure can be viewed in the online issue, which is available at wileyonlinelibrary.com.]

independent study[11] using a different DPM-CFD code. How cohesion affects the pressure drop behavior near U_{mf} will be explored further when examining the effects of friction.

Observations reveal that the extent of hysteresis also increases when the effects of cohesion are included. In agreement with experimental observations,[47] the pressure drop curve during defluidization lies well below that for fluidization, whereas the opposite is observed for bed height. Note that, the bed height curve corresponding to defluidization lies above that of fluidization except at low superficial gas velocities ($U_{sf} < U_{mf}$). Below this point, the curves cross, indicating a slightly more compact bed in the final stage of the defluidization cycle compared to the initial stage of the fluidization cycle. This behavior suggests the bed did not reach its maximum random packing prior to the fluidization stage and is attributed to the rapid rate of defluidization that follows the initial fluidization at approximately 1.2 U_{mf}. Experimentally, when a bed of Geldart A particles is defluidized at the same rate, the bed height during defluidization is generally found to lie above that of fluidization. This behavior is attributed to the existence of yield stresses in the bed.[47] For example, when cohesion is included (see Figure 3), the behavior follows the experimentally observed trend more closely. Namely, the bed height during defluidization tends to lie above or near the height during fluidization for all U_{sf}. In a cohesive system, the particles derive more support from the forces transmitted through the assembly to the distributor and walls during defluidization, and there is greater frictional resistance,[47] which acts to slow particle settling (resist compression) compared to a noncohesive system.

The minimum fluidization and bubbling velocities are seen to increase slightly compared to the noncohesive case. This behavior is in slight contrast to earlier DPM-CFD simulation studies, which have reported an increase in U_{mb} but not U_{mf} with the addition of interparticle forces.[36,46,49] In this study, the slight increase in the value of U_{mf} can be explained by the increase in bed height at U_{mf}, which corresponds to a less packed bed. This result indicates that the predicted U_{mf} is sensitive to the computed porosity of the bed, which is lower in the noncohesive case. Such behavior is reasonable as the calculated drag force at U_{mf} is sensitive to the predicted porosity at these conditions, which in turn is sensitive to frictional forces, as explained in the next section.

A simple quantitative check of the computed values for the minimum fluidization and bubbling velocities is possible by comparison with values estimated from available empirical correlations. For example, using the correlations recommended by Abrahamsen and Geldart[50] and the physical properties listed in Table 1, U_{mf} and U_{mb} are calculated as 0.35 and 0.70 cm/s, respectively. As evident, the computed values of U_{mf} and U_{mb} (see, for example, Figure 3) are higher than those calculated from the correlation. The overestimate is attributed to the predicted porosities at these conditions, which is also affected by the nature of the powder, such as polydispersity and friction as will be described later. Furthermore, the predicted values of U_{mf} and U_{mb} will depend on the selected drag correlation. Abrahamsen and Geldart[50] also present a simple empirical correlation for the bed expansion as $H_{mb}/H_{mf} = (U_{mb}/U_{mf})^{0.22}$. A value of 1.11 is obtained using this correlation, which is identical to the value calculated from the bed expansion height presented in Figure 3.

To illustrate the fluidization/defluidization behavior of the simulated fluidized bed, snapshots of this cohesive system are shown in Figures 4a, b gives the corresponding results from a polydisperse case with a PSD, which will be discussed in more detail below. To better visualize the bed behavior, only a thin slice of the 3-D system, approximately three to four particle diameters thick, in the xy-plane centered at $z/d_p = 20$ is displayed. Particles are colored according to the magnitude of the dimensionless total cohesive force ($F_{vw}^* = F_{vw,p}/mg$). During the initial fluidization cycle ($U_{sf} <= \sim U_{mf}$), the bed consists of particles in contact with a range of interparticle attractive forces (left most pane). At $U_{sf} \sim 2\ U_{mf}$, the overall level of cohesion exhibited in the system is less. In regard to the monodisperse case (Figure 4a), 2 U_{mf} exceeds U_{mb}, and hence the bed has expanded and bubbling is observed. The magnitude of cohesive bonds continues to diminish with increasing gas velocity as the bed expands (Figure 3) and bubbles more vigorously (middle pane Figure 4). If the gas velocity is further increased, then a slugging regime will develop due to the small geometry of the bed. On decreasing the superficial gas velocity, the bed behavior closely reflects the behavior observed when gas velocity was increased, although bubbling is maintained through lower U_{sf} and the bed remains slightly more expanded.

Snapshots corresponding to the 12 species polydisperse system show a few noteworthy differences with the monodisperse case. Recall that the simulation setup for the polydisperse case differs slightly from the monodisperse case in that the initial fluidization occurs over a longer period (1 s). This period allows particles with different sizes to naturally segregate as shown in Figure 4b. In particular, the larger particles form a conical pile near the bottom of the bed, whereas a higher concentration of fines is noticeable toward the top and near the walls, evident in the large-scaled cohesive forces. Note that, these larger particles exhibit relatively lower cohesive forces compared to the smaller particles because the illustrated particle cohesive force is scaled by the respective particle weight. Also, compared to the monodisperse case, bubbles are still not forming in the fluidization of the polydipserse powder at a superficial gas velocity U_{sf} $\sim 2\ U_{mf}$. Two factors likely contribute to the delay in bubbling: (1) the large pile of coarse particles that forms at the bottom of the bed and are difficult to fluidize because of

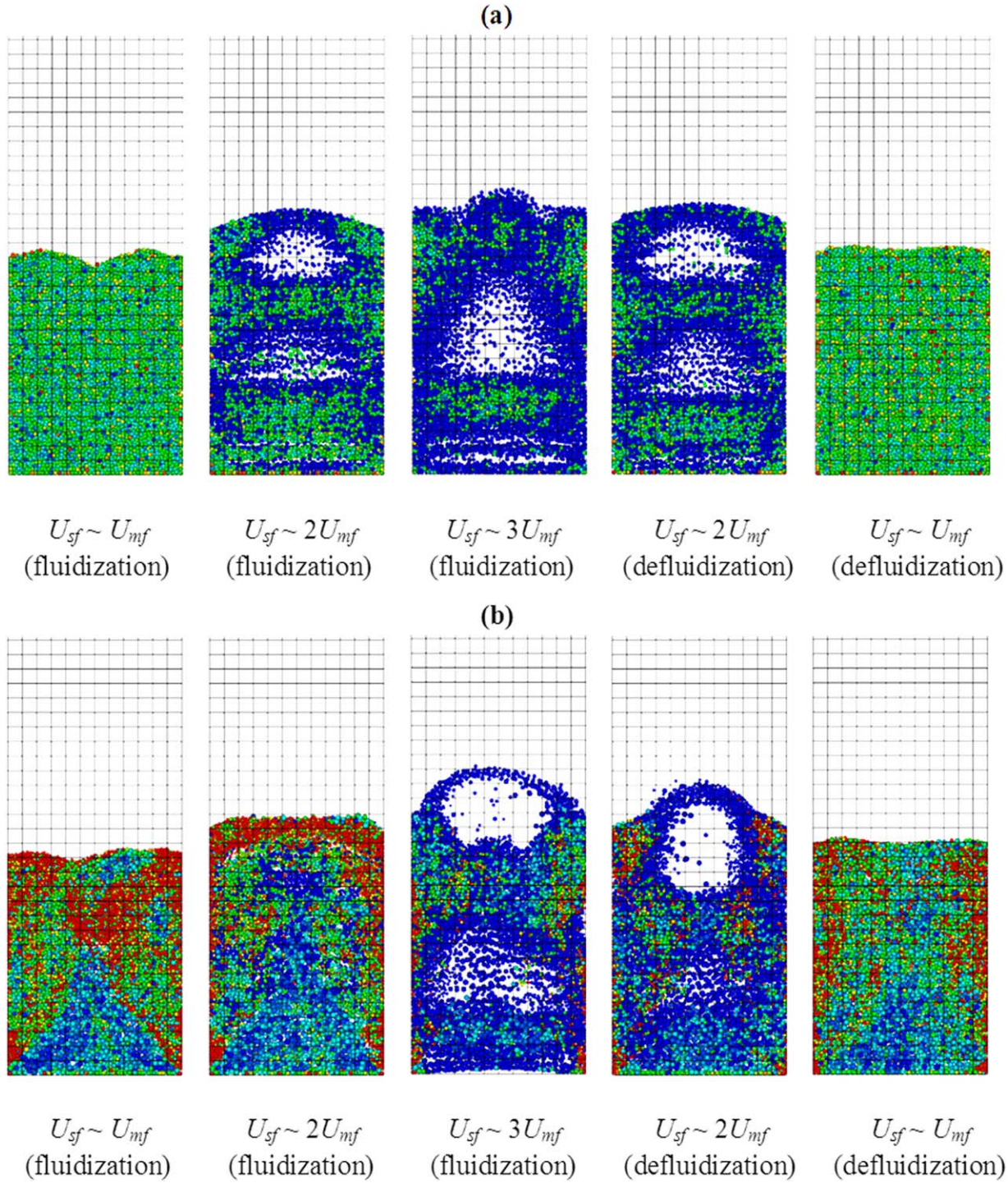

Figure 4. Snapshots showing bed behavior at varying intervals during the fluidization/defluidization cycle for the (a) monodisperse and the (b) 12 species polydisperse system.

Other physical parameters as in Figure 3. Particles are colored by the magnitude of cohesive forces made dimensionless with weight of particles (red and blue indicate values larger than 4 and near zero, respectively). Shown is only a thin slice of the 3-D domain that is about three to four particles diameter in the *xy*-plane. [Color figure can be viewed in the online issue, which is available at wileyonlinelibrary.com.]

their mass and (2) the high concentration of fines at the top of the bed form large cohesive clusters, which are also difficult to fluidize. These observations reflect the occurrence of segregation of particles by size, which occurred in the bed during the fluidization process with large particles settling at the bottom and higher concentration of smaller particles at the top of the bed. Finally, a comparison of the snapshots near U_{mf} during fluidization and defluidization (left and right most panes of Figure 4b indicate that the state of a bed composed of polydisperse powders has varied in this first fluidization/defluidization cycle. Experimentally, the first few cycles are generally ignored (e.g., Tsinontides and Jackson[47]). Computationally, however, simulating several cycles becomes extremely expensive. Therefore, this study is

limited to the first cycle, which experimentally has been found to show the largest pressure-overshoot.[51]

Effect of Friction

To gauge the importance of frictional effects in regard to the presence of a pressure overshoot at U_{mf}, simulations were run with varying levels of friction. Variations in friction coefficient are due to different surface properties that can be caused by either different materials (e.g., glass beads vs. FCC particles) or by particles fluidized under different conditions (e.g., lubrication effects due to high humidity). The results are displayed in Figure 5a for μ of 0, 0.01, and 0.1. (The results corresponding to μ of 0.3 are presented in Figure 3.) These results may also be coupled with those of Figure 2, the same system but with $\mu = 0.3$ and $A = 0$ (i.e., friction but no cohesion), to form a more complete picture. Comparing Figure 3 to that of Figure 2, which have the same friction but are with and without cohesion, respectively, shows that the pressure overshoot at U_{mf} is nominal without cohesion. In addition, the pressure overshoot is insignificant when cohesion is present but friction is removed (Figure 5a for $\mu = 0$) and a slight increase in μ from 0 to 0.01 still results in an insignificant pressure overshoot. Only when μ is further increased to 0.1 does the pressure overshoot become visible, indicating that relatively large values of friction are necessary to predict this behavior. In aggregate, this evidence indicates that friction is responsible for the pressure overshoot at U_{mf} only when particles are held closely together by the interparticle attractive force. In other words, cohesion keeps particles together and allows the effects of friction to manifest. This conclusion may be further considered in the context of these two limiting cases: (1) turn off cohesion and ramp up friction and (2) turn off friction and ramp up cohesion. In regard to the first case, a significant pressure overshoot was not observed even when friction was increased;[48] that is, without cohesion the level of friction was effectively inconsequential. Note that, this analysis only concerns small type A spherical particles in a packed-bed arrangement. For heavier and/or nonspherical particles for which cohesive forces can be neglected, this behavior can still be observed (e.g., see Kunii and Levenspiel[7]). In regard to the second case, an increase in cohesion (without friction) will result in shifting the particle classification from Geldart group A to group C. Recall group C describes powders that are in any way cohesive and are characterized as extremely difficult to fluidize.[1]

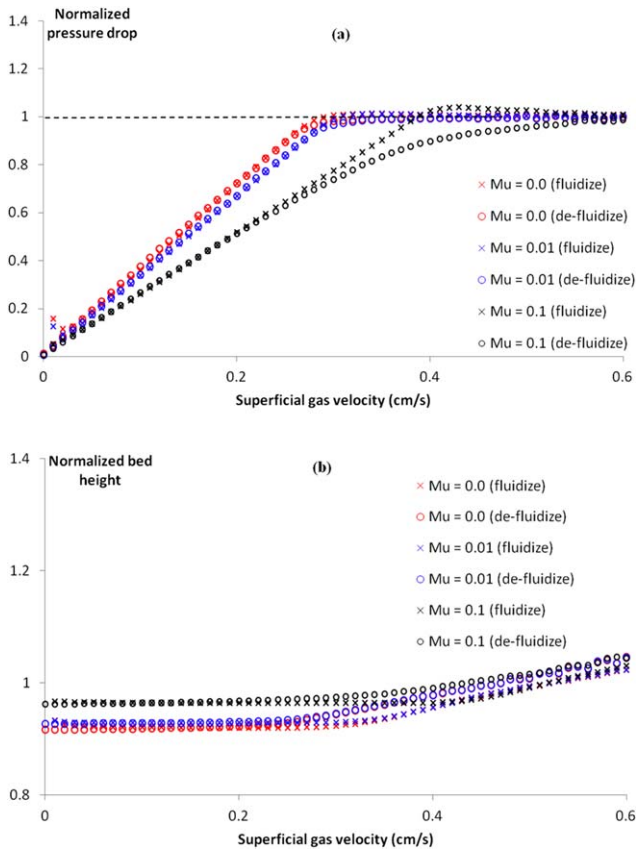

Figure 5. Effect of friction on the fluidization/defluidization curves of a cohesive monodisperse powder (a) the normalized pressure drop and (b) bed height.

Other properties as in Figure 3. [Color figure can be viewed in the online issue, which is available at wileyonlinelibrary.com.]

Figure 5 also reveals that the minimum fluidization velocity increases as the level of friction increases. Accordingly, frictionless particles result in the smallest U_{mf}. This can be traced to the overall bed packing density. Specifically, Figure 5b shows the corresponding nondimensional bed heights during fluidization. In particular, the nondimensional bed heights of less than one, corresponding to $\mu = 0$ and $\mu = 0.01$, indicate denser beds relative to $\mu = 0.1$. The fact that decreasing friction results in lower void fraction has been observed in previous studies.[52] Finally, the hysteresis in the fluidization and defluidization pressure drop curves becomes more prominent with higher values of friction. These observations are in agreement with a simple model proposed by Jackson[6], who observed that friction is the main cause of the pressure drop overshoot and the increased hysteresis near U_{mf}. The present study reinforces this earlier work and augments it with the observation that, for small Geldart A particles, cohesion is necessary to reveal the effects of the frictional forces.

Effect of PSD

Up to now, the influence of van der Waals cohesive forces on the fluidization behavior of Geldart A particles has been examined in the context of a powder defined by a single particle size. Particles in a real powder will seldom be of uniform size but will be characterized by a PSD, which will impact their rheological and fluidization behavior. For example, a wide size distribution has been observed to lead to smoother fluidization and better gas-solid contacting,[53] whereas a narrow distribution may enhance bed stability (e.g., reduce segregation).[54] In addition, the presence of fines (particles of 45-μm diameter or less) may improve the performance of fluidized-bed reactors;[55,56] however, excessive fines may cause the powder to be too cohesive for proper fluidization.[57]

Particle size and PSD will influence the magnitude of the interparticle force. In view of this, the impact of van der Waals cohesive forces on the fluidization behavior is also investigated in the context of two powders having different PSD but the same mean diameter of about 75 μm (see Table 2). The results are presented in Figures 6 and 7, characterized by three and 12 different particle sizes, respectively. As the size distribution increases, the minimum fluidization

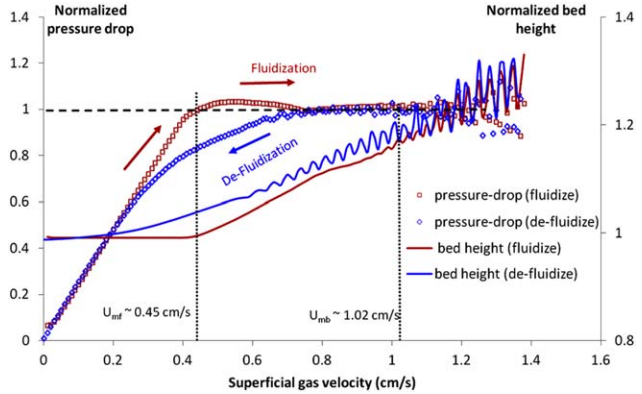

Figure 6. Fluidization/defluidization curves of a cohesive polydisperse powder characterized by three solids species of different particle size but same density.

Mean particle diameter and other properties as in Figure 3. [Color figure can be viewed in the online issue, which is available at wileyonlinelibrary.com.]

velocity decreases, while the minimum bubbling velocities increases. Specifically, U_{mf} is 0.55, 0.45 cm/s, and 0.41 cm/s for the monodisperse, three and 12 species cases, respectively, whereas the corresponding U_{mb} is 0.87, 1.02, and 1.07 cm/s. The data clearly shows that homogeneous expansion occurs over a larger range of superficial gas velocities for the polydisperse cases compared to the monodisperse case (see Figure 3). This result is mainly due to the increase in the minimum bubbling velocity, which is attributed to the segregation of large, more massive particles at the bottom of the bed and highly cohesive fines at the top and near the walls of the bed (discussed earlier in reference to Figure 4). Conversely, the minimum fluidization velocity is primarily affected by the predicted void fraction, which, as evident from the decreases in bed height, decreases slightly as the PSD becomes wider. This behavior is explained by considering the nature of the packed bed; that is, smaller particles may occupy some of the voids formed by larger particles

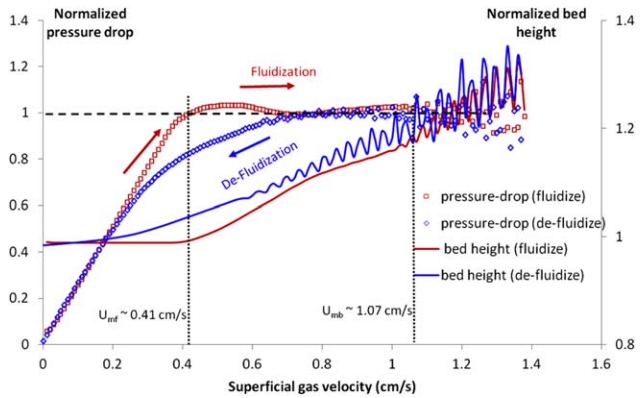

Figure 7. Fluidization/defluidization curves of a cohesive powder characterized by a realistic particle-size distribution obtained using 12 solids species.

Mean particle diameter and other properties as in Figure 3. [Color figure can be viewed in the online issue, which is available at wileyonlinelibrary.com.]

and may produce a significant decrease in the void fraction in a bed characterized by a PSD.[58] In this study, the particles are allowed to naturally segregate under gravity prior to the fluidization cycle, and as a result, such extreme changes in packing values were not predicted. Finally, unlike the monodisperse case, the minimum fluidization for polydisperse cases does not occur at the maximum pressure drop overshoot but rather at the point where the pressure drop first balances the weight of the bed. Recall that the definition of minimum fluidization velocity in this study corresponds to the point where a change in slope of the bed height curve is observed indicating bed expansion. These qualitative and quantitative differences in the fluidization behavior of powders with PSD indicate that they cannot be accurately simulated with a single particle size. As indicated by comparing both Figures 6 and 7, however, simulating the full-experimental PSD with either three or 12 particle diameters results in similar fluidization behavior. This analysis gives further validity to a recent study in the literature based on a continuum kinetic theory model[59] that found fewer particle diameters may be used to accurately represent a full PSD.

Conclusions

This study investigated the effects of cohesive forces on the fluidization/defluidization of small type A powders using a discrete particle approach. Significant changes in the fluidization behavior are predicted when cohesion is included in simulations. Namely, the spike in pressure drop and hysteresis around minimum fluidization are quantitatively more noticeable. In the literature, these observed phenomena have been previously attributed to friction. The main contribution of this study is to explain how contact friction occurs in small particles during fluidization. In particular, this investigation demonstrates that the main role of interparticle cohesive forces is to maintain close contact among particles. As a result, the effects of sliding friction between particles and between particles and walls are emphasized in the presence of cohesion. The present results show that without the effects of cohesion, the action of friction is minimal for small type A particles.

The effects of including a real PSD as well as a simplified PSD with much fewer particle sizes were also studied. Quantitative differences between the fluidization of monodisperse and polydisperse powders are observed. Namely, when a PSD is considered, a wider range of homogeneous fluidization is observed, with both lower minimum fluidization and higher minimum bubbling velocities, which is attributed to the axial segregation of particles by size that occurs in the system with a PSD. Therefore, if only a single-particle size is considered, then the corresponding results will be inaccurate when compared with those from the full PSD of 12 particle sizes. Then again, this study also shows that reasonable results may still be achieved when considering only three particle sizes. Although this conclusion may not be relevant to a DPM approach, it is of major consequence to most continuum-type models based on the kinetic theory of granular flow because it shows that fewer solids species may need to be considered, which may lead to significant computational savings.

Literature Cited

1. Geldart D. Types of gas fluidization. *Powder Technol.* 1973;7(5):285–292.

2. Khoe GK, Ip TL, Grace JR. Rheological and fluidization behavior of powders of different particle-size distribution. *Powder Technol.* 1991;66(2):127–241.
3. Molerus O. Interpretation of Geldart's type A, B, C and D powders by taking into account interparticle cohesion forces. *Powder Technol.* 1982;33(1):81–87.
4. Royer JR, Evans DJ, Oyarte L, Guo Q, Kapit E, Mobius ME, Waitukaitis SR, Jaeger HM. High-speed tracking of rupture and clustering in freely falling granular streams. *Nature*. 2009;459(7250): 1110–1113.
5. Girimonte R, Formisani B. The effects of thermally induced interparticle forces on the expansion and bubbling behavior of a fluidized bed. In: Berruti F, Bi X, Pugsley T, editors. *The 12th International Conference on Fluidization—New Horizons in Fluidization Engineering*. Vancouver, Canada: ECI Digital Archives, 2007:177–184.
6. Jackson R. The *Dynamics of Fluidized Particles*. New York, NY: Cambridge University Press, 2000.
7. Kunii D, Levenspiel O. *Fluidization Engineering*, *2nd ed.* Boston: Butterworth-Heinemann, 1991.
8. Gidaspow D, Huilin L. Equation of state and radial distribution functions of FCC particles in a CFB. *AIChE J*. 1998;44(2):279–293.
9. van Wachem B, Sasic S. Derivation, Simulation and validation of a cohesive particle flow CFD model. *AIChE J*. 2008;54(1):9–19.
10. Ye M, van der Hoef MA, Kuipers JAM. From discrete particle model to a continuous model of Geldart A particles. *Chem Eng Res Des*. 2005;83(A7):833–843.
11. Pandit JK, Wang XS, Rhodes MJ. Study of Geldart's Group A behaviour using the discrete element method simulation. *Powder Technol.* 2005;160(1):7–14.
12. Pandit JK, Wang XS, Rhodes MJ. On Geldart Group A behaviour in fluidized beds with and without cohesive interparticle forces: a DEM study. *Powder Technol.* 2006;164(3):130–138.
13. Rhodes MJ, Wang XS, Nguyen M, Stewart P, Liffman K. Onset of cohesive behaviour in gas fluidized beds: a numerical study using DEM simulation. *Chem Eng Sci*. 2001;56(14):4433–4438.
14. Wang JW, van der Hoef MA, Kuipers JAM. The role of scale resolution versus inter-particle cohesive forces in two-fluid modeling of bubbling fluidization of Geldart A particles. *Chem Eng Sci*. 2011; 66(18):4229–4240.
15. Wang J, van der Hoef MA, Kuipers JAM. The role of particle-particle interactions in bubbling gas-fluidized beds of Geldart A particles: a discrete particle study. In: Guo L, Jospeh DD, Matsumoto Y, Sommerfeld Y, Wang Y, editors. *6th International Symposium on Mulitphase Flow, Heat Mass Transfer and Energy Conversion*, Xi'an, China: AIP Conference Proceedings, 2009:766.
16. Hamaker HC. The London-van der Waals attraction between spherical particles. *Physica*. 1937;4(10):1058–1072.
17. Hiemenz PC. *Principles of Colloid and Surface Chemistry*, *2nd ed.* New York: Marcel Dekker, 1986.
18. Israelachvili JN. *Intermolecular and Surface Forces*, *3rd ed.* Academic Press, Waltham, MA, USA, 2011.
19. Wen CY, Yu YH. *Mechanics of Fluidization*. New York: American Institute of Chemical Engineers, 1966.
20. Cundall PA, Strack ODL. A discrete numerical model for granular assemblies. *Geotechnique*. 1979;29(1):47–65.
21. Garg R, Galvin J, Li T, Pannala S. Open-source MFIX-DEM software for gas-solids flows: partice I-verification. *Powder Technol.* 2012;220(1):122–137.
22. Castellanos A. The relationship between attractive interparticle forces and bulk behaviour in dry and uncharged fine powders. *Adv Phys*. 2005;54(4):263–376.
23. Visser J. An invited review: van der Waals and other cohesive forces affecting powder fluidization. *Powder Technol*. 1989;58(1):1–10.
24. Rabinovich YI, Adler JJ, Ata A, Singh RK, Moudgil BM. Adhesion between nanoscale rough surfaces. *J Colloid Interface Sci*. 2000; 232(1):10–16.
25. Adams GG, Nosonovsky M. Contact modeling—forces. *Tribology Int*. 2000;33(5–6):431–442.
26. Rumpf H. *Particle Technology*. New York: Chapman and Hall, 1990.
27. Dzyaloshinskii IE, Lifshitz EM, Pitaevskii LP. The general theory of van der Waals forces. *Adv Phys*. 1961;38(10):165–209.
28. Lifshitz EM. The theory of molecular attractive forces between solids. *Sov Phys JETP*. 1956;2(1):73–83.
29. Tomas J. Mechanics of nanoparticle adhesion: a continuum approach. In: Mittal KL, editor. *8th International Symposium on Particles on Surfaces: Detection*, Adhesion and Removal, Providence, Rhode Island: CRC Press, 2002:1–47.
30. Li Z, Yang J, Xu X, Xu X, Yu W, Yue X, Sun C. Particle shape characteriziation of fluidized catalytic cracking catalyst powders using the mean value and distribution of shape factors. *Adv Powder Technol*. 2002;13(3):249–263.
31. Forsyth AJ, Rhodes MJ. A simple model incorporating the effects of deformation and asperities into the van der Waals force for macroscopic spherical solid particles. *J Colloid Interface Sci*. 2000;223(1): 133–138.
32. Xie HY. The role of interparticle forces in the fluidization of fine particles. *Powder Technol*. 1997;94(2):99–108.
33. Massimilla L, Donsi G. Cohesive forces between particles of fluid-bed catalysts. *Powder Technol*. 1976;15(2):253–260.
34. Patankar SV. *Numerical Heat Transfer and Fluid Flow*. India: Taylor & Francis, 1980.
35. Guenther C, Syamlal M. The effect of numerical diffusion on simulation of isolated bubbles in a gas-solid fluidized bed. *Powder Technol*. 2001;116(2–3):142–154.
36. Ye M, van der Hoef MA, Kuipers JAM. The effects of particle and gas properties on the fluidization of Geldart A particles. *Chem Eng Sci*. 2005;60(16):4567–4580.
37. Knowlton T, Geldart D, Matsen J, King D. Comparison of CFB Hydrodynamic Models. *PSRI Challenge Problem—Presented at the Eighth International Fluidization Conference*. Tour, France, 1995.
38. Shafer J, Dippel S, Wolf DE. Force schemes in simulations of granular materials. *J Phys I Fr*. 1996;6(1):5–20.
39. Tsuji Y, Kawaguchi T, Tanaka T. Discrete particle simulation of two-dimensional fluidized bed. *Powder Technol*. 1993;77(1):79–87.
40. Silbert LE, Ertas D, Grest GS, Halsey TC, Levine D, Plimpton SJ. Granular flow down an inclined plane: bagnold scaling and rheology. *Phys Rev E*. 2001;64(5):1–14.
41. Chirone R, Massimilla L, Russo S. Bubble-free fluidization of a cohesive powder in an acoustic field. *Chem Eng Sci*. 1993;48(1): 41–52.
42. Syamlal M, O'Brien TJ. Fluid dynamic simulation of O3 decomposition in a bubbling fluidized bed. *AIChE J*. 2003;49(11):2793–2801.
43. Goldschmidt MJV, Link JM, Mellema S, Kuipers JAM. Digital image analysis measurements of bed expansion and segregation dynamics in dense gas-fluidised beds. *Powder Technol*. 2003;138 (2–3):135–159.
44. Xu BH, Zhou YC, Yu AB, Zulli P. Force structures in gas fluidized beds of fine powders. *World Congress on Particle Technology 4*. Sydney, Australia: Technical Committee, 2002.
45. Ye M, van der Hoef MA, Kuipers JAM. A numerical study of fluidization behavior of Geldart A particles using a discrete particle model. *Powder Technol*. 2004;139(2):129–139.
46. Rhodes MJ, Wang XS, Nguyen M, Stewart P, Liffman K. Use of discrete element method simulation in studying fluidization characteristics: influence of interparticle force. *Chem Eng Sci*. 2001;56(1): 69–76.
47. Tsinontides SC, Jackson R. The mechanics of gas-fluidized beds with an interval of stable fluidization. *J Fluid Mech*. 1993;255:237–274.
48. Weber MW, Hrenya CM. Computational study of pressure-drop hysteresis in fluidized beds. *Powder Technol*. 2007;177(3):170–184.
49. Kobayashi T, Mukai T, Kawaguchi T, Tanaka T, Tsuji Y. DEM Analysis on Flow Patterns of Geldart's Group A Particles in Fluidized Bed. *World Congress on Particle Technology 4*. Sydney, Australia: Technical Committee, 2002.
50. Abrahamsen AR, Geldart D. Behavior of gas-fluidized beds of fine powders part I. Homogeneous expansion. *Powder Technol*. 1980;26: 35–46.
51. Tucker J. Private communication. In: Benyahia S, editor. Discussion of Experimental Fluidization Curves of Polydisperse Powders Measured at NETL and their Repeatability,
52. Zhang ZP, Liu LF, Yuan YD, Yu AB. A simulation study of the effects of dynamic variables on the packing of spheres. *Powder Technol*. 2001;116(1):23–32.
53. Grace JR, Sun G. Influence of particle-size distribution on the performance of fluidized-bed reactors. *Can J Chem Eng*. 1991;69(5): 1126–1134.
54. Gautheir D, Zerguerras S, Flamant G. Influence of the particle size distribution of powders on the velocities of minimum and complete fluidization. *Chem Eng J*. 1999;74(1):181–196.
55. Pell M, Jordan SP. Effects of fines and velocity on fluid bed reactor performance. *AIChE Symp Ser*. 1988;84(262):68–73.
56. Yates JG, Newton D. Fine particle effects in a fluidized-bed reactor. *Chem Eng Sci*. 1986;41(4):801–806.

57. Geldart D. The effect of particle size and size distribution on the behaviour of gas-fluidised beds. *Powder Technol*. 1972;5(4):201–215.
58. Yu AB, Bridgwater J, Burbidge A. On the modelling of the packing of fine particles. *Powder Technol*. 1997;92(3):185–194.
59. Murray JA, Benyahia S, Metzger P, Hrenya CM. Continuum representation of a continuous size distribution of particles engaged in rapid granular flow. *Phys Fluids*. 2012;24(8):083303–083322.

Manuscript received July 22, 2013, and revision received Nov. 7, 2013.